JPE 17-2-6

https://doi.org/10.6113/JPE.2017.17.2.368
ISSN(Print): 1598-2092 / ISSN(Online): 2093-4718

Torque Ripple Reduction in Three-Level Inverter-Fed Permanent Magnet Synchronous Motor Drives by Duty-Cycle Direct Torque Control Using an Evaluation Table

Wei Chen[†], Ying-Ying Zhao[*], Zhan-Qing Zhou[*], Yan Yan[*], and Chang-Liang Xia[*,**]

[†,*]School of Electrical and Information Engineering, Tianjin University, Tianjin, China
[**]Tianjin Engineering Center of Electric Machine System Design and Control, Tianjin, China

Abstract

In this paper, a direct torque control algorithm with novel duty cycle-based modulation is proposed for permanent magnet synchronous motor drives fed by neutral-point clamped three-level inverters. Compared with the standard DTC, the proposed algorithm can suppress steady-state torque ripples as well as ensure neutral-point potential balance and smooth vector switching. A unified torque/flux evaluation table with multiple voltage vectors and precise control levels is established and used in this method. This table can be used to evaluate the effects of duty-cycle vectors on torque and flux directly, and the elements of the table are independent of the motor parameters. Consequently, a high number of appropriate voltage vectors and their corresponding duty cycles can be selected as candidate vectors to reduce torque ripples by looking up the table. Furthermore, small vectors are incorporated into the table to ensure the neutral-point potential balance with the numerous candidate vectors. The feasibility and effectiveness of the proposed algorithm are verified by both simulations and experiments.

Key words: Direct torque control, NPC three-level inverter, Permanent magnet synchronous motor, Torque ripple reduction

I. INTRODUCTION

The main advantages of permanent magnet synchronous motor (PMSM) are their simple structure, good reliability, and high power density. PMSMs are widely used in the fields of rail traction and wind power generation [1], [2]. Neutral-point-clamped three-level inverters (3L-NPCs) have been used in medium-power applications because these inverters present low harmonic contents in the output voltage and current and low stress on the semiconductors [3]-[5]. Thus, PMSM drives fed by 3L-NPCs have broad application prospects.

Direct torque control (DTC) is one of the main control algorithms for a PMSM drive fed by a three-level inverter (3L-DTC). The merits of DTC include rapid torque response, simple structure (DTC does not require complex coordinate transformation and current regulation), and motor-parameter independence [6], [7]. However, the standard 3L-DTC exhibits large torque ripples due to two reasons. First, the standard 3L-DTC adopts the structure of hysteresis controllers and switching tables, and only large and medium voltage vectors are employed to control the torque and flux [8], [9]. Second, constrained by the topology of the 3L-NPC, the output vector selection should consider the neutral-point balance and smooth vector switching [5], [10]. A neutral-point potential unbalance causes low-order harmonics in the output voltage, and these harmonics consequently lead to low-frequency torque fluctuations. Unsmooth vector switching means a direct "jump" between the positive and negative buses in a phase voltage, reducing both the quality of the output voltage and the accuracy of the control.

Numerous improved algorithms have been proposed in the literature [8]-[16] to solve the problem of torque ripples in the

Manuscript received Jul. 14, 2016; accepted Jan. 23, 2017
Recommended for publication by Associate Editor Dong-Myung Lee.
[†]Corresponding Author: chen_wei@tju.edu.cn
Tel: +86-22-27402325, Fax: +86-22-27402325, Tianjin University
[*]School of Electrical and Information Engineering, Tianjin University, China
[**]Tianjin Engineering Center of Electric Machine System Design and Control, China

standard 3L-DTC. These algorithms can be divided into single vector-based DTC (SV-DTC), DTC with discrete space vector modulation (DSVM-DTC), and duty cycle-based DTC (DC-DTC) according to the vector output mode. SV-DTC improves torque control precision by merging small vectors into a switching table and then suppressing the steady torque ripples [12], [13]. In [12], the relationship between the stator current ripples and the flux vector was analyzed when a motor operates in the steady state. The results showed that the current ripples were reduced by utilizing small vectors; thus, a novel switching table that contains small vectors was established to achieve minimum current ripples [12]. In [13], the conventional torque hysteresis controller was improved as a four-level torque controller by combining small vectors. This 3L-DTC algorithm can achieve torque ripple reduction and constant switching frequency. DSVM-DTC employs several virtual voltage vectors to control a motor. These vectors are synthesized by a modulation technique, and they have fixed direction and amplitude. In [8], each control period was divided into 9 short intervals, and 12 virtual vectors with constant amplitude were distributed uniformly in the fixed-angle space and synthesized by adopting a single basic vector in each interval. Similarly, 24 virtual vectors were synthesized by space vector pulse width modulation (SVPWM) in [14], and the stator flux sectors were subdivided into 24 regions. In each region, the torque ripples can be kept within a narrow range by outputting a virtual vector on the basis of the control errors of the torque and flux. DC-DTC employs several basic voltage vectors in each control period. The duration of these basic vectors are calculated in accordance with the criterion of the minimum torque ripples [15], [16]. In [16], the switching table and the torque hysteresis controller were redesigned, and two voltage vectors were used to control the motor. The first basic voltage vector was selected on the basis of the switching table, and the second voltage vector was generated using the predicted duty cycle based on the mathematical model of the motor.

To achieve the neutral-point potential balance and smooth vector switching of 3L-DTC on the premise of excellent torque performance, SV-DTC adopts the intermediate vector method [13], [8], whereas DSVM-DTC adopts the fixed synthesis vector method [9], [14]. However, the corresponding method for DC-DTC has not been discussed in the literature. The intermediate vector method employs the adjacent medium (large) vector instead of the original vector selected by the switching table to avoid switching directly between large (medium) vectors. This method measures the neutral-point potential in real time, and the adjacent small vectors are used as intermediate vectors to balance the neutral-point potential. This method can degrade the performance of torque and increase the complexity of vector selection given that the intermediate vectors are different from the original output vectors selected by the switching table. The fixed synthesis vector method

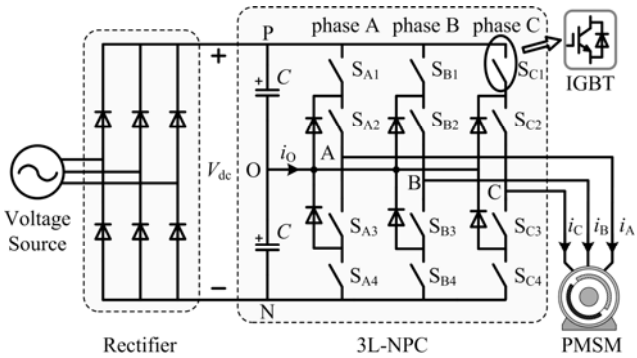

Fig. 1. Main circuit of a 3L-NPC.

TABLE I
S_A STATES OF INSULATED GATE BIPOLAR TRANSISTORS (IGBTS) AND V_{AN}

S_A	States of IGBTs	V_{AN}
0	S_{A1} and S_{A2} off; S_{A3} and S_{A4} on	0
1	S_{A2} and S_{A3} on; S_{A1} and S_{A4} off	$V_{dc}/2$
2	S_{A1} and S_{A2} on; S_{A3} and S_{A4} off	V_{dc}

simultaneously utilizes the two different switching states of the same small vector in each control period. The neutral-point potential balance can be achieved using this method by adjusting the switching time of the two switching states. This method always employs the same zero vector at the start and end of each control period considering the smooth vector switching.

A novel duty cycle-based DTC algorithm is proposed in this paper. In the proposed algorithm, a unified torque/flux evaluation table for 3L-DTC is established. The control effects of all the basic and virtual vectors on the torque and flux can be evaluated directly with this table. Subsequently, the appropriate vectors that can achieve smooth torque and flux control are selected to control the PMSM. The control effects of the small vectors have already been incorporated into the evaluation table to ensure neutral-point potential balance and smooth vector switching of 3L-NPC. Therefore, the neutral-point potential balance can be achieved by utilizing the small vectors directly instead of inserting an additional intermediate vector. The smooth vector switching is attained by starting and ending with the same zero vectors in each control period.

II. STANDARD 3L- DTC

A. Model of a 3L-NPC

A schematic of a typical PMSM drive fed by a 3L-NPC is presented in Fig. 1, where i_O denotes the neutral-point current; i_A, i_B, and i_C denote the three-phase currents of the PMSM; and V_{dc} denotes the DC-link voltage.

The switching function S_j ($j \in \{A, B, C\}$) is introduced to describe the states of the four switching devices of each phase. For example, for phase A, the values of S_A and the voltage V_{AN} are listed in Table I.

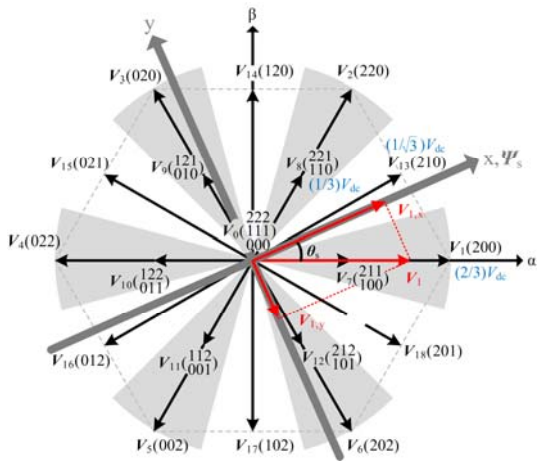

Fig. 2. Voltage vectors of 3L-NPC.

The switching state of each voltage vector can be represented by $S_AS_BS_C$. A total of 27 switching states correspond to 19 basic vectors, as shown in Fig. 2. These basic vectors can be divided into zero vectors (ZV, $\boldsymbol{V}_0$), large vectors (LV, $\boldsymbol{V}_1$–$\boldsymbol{V}_6$), small vectors (SV, $\boldsymbol{V}_7$–$\boldsymbol{V}_{12}$), and medium vectors (MV, $\boldsymbol{V}_{13}$–$\boldsymbol{V}_{18}$), whose amplitudes are 0, $(2/3)V_{dc}$, $(1/3)V_{dc}$, and $(1/\sqrt{3})V_{dc}$, respectively.

B. Basic Principles of PMSM-DTC

The x–y rotating coordinate system is established in Fig. 2, where the stator flux vector $\boldsymbol{\Psi}_s$ is oriented and aligned on the x-axis, and θ_s is the phase angle of $\boldsymbol{\Psi}_s$. The stator voltage equation of the PMSM in the x–y rotating coordinate system can be expressed as follows [17]:

$$\begin{cases} V_{n,y} = R_s i_y + \omega_s |\boldsymbol{\Psi}_s| \\ V_{n,x} = R_s i_x + \dfrac{d}{dt}|\boldsymbol{\Psi}_s| \end{cases} \tag{1}$$

where n = 0, 1, . . . , 18 denotes the numbers of the voltage vectors; $V_{n,x}$ and $V_{n,y}$ are the projections on the x-axis and y-axis of $\boldsymbol{V}_n$, respectively; i_x and i_y are the projections on the x-axis and y-axis of $\boldsymbol{I}$, respectively; and $|\boldsymbol{\Psi}_s|$, ω_s, and R_s are the stator flux amplitude, electrical angular velocity, and stator resistance, respectively.

The torque change rate of the PMSM can be expressed as

$$\frac{d}{dt}T_e = \frac{3p|\boldsymbol{\Psi}_s|}{2L_dL_q}\left[\psi_f L_q \cos\delta - |\boldsymbol{\Psi}_s|\left(L_q - L_d\right)\cos 2\delta\right]\frac{d\delta}{dt} \tag{2}$$

where p, L_d, L_q, and ψ_f denote the pole pair number, direct stator inductance, quadrature stator inductance, and permanent magnet flux, respectively; and δ is the displacement angle between the stator and permanent magnet flux linkage. The change rate of δ is given by

$$\frac{d\delta}{dt} = \frac{d\left(\theta_s - \theta_r\right)}{dt} = \omega_s - \omega_r \tag{3}$$

where θ_r and ω_r are the rotor position and rotor electrical angular velocity, respectively.

TABLE II
SWITCHING TABLE OF A STANDARD 3L-DTC

C_Ψ	C_T	Stator Flux Sectors, h_θ											
		1	2	3	4	5	6	7	8	9	10	11	12
+1	+1	$\boldsymbol{V}_2$	$\boldsymbol{V}_{14}$	$\boldsymbol{V}_3$	$\boldsymbol{V}_{15}$	$\boldsymbol{V}_4$	$\boldsymbol{V}_{16}$	$\boldsymbol{V}_5$	$\boldsymbol{V}_{17}$	$\boldsymbol{V}_6$	$\boldsymbol{V}_{18}$	$\boldsymbol{V}_7$	$\boldsymbol{V}_{13}$
	−1	$\boldsymbol{V}_6$	$\boldsymbol{V}_{18}$	$\boldsymbol{V}_1$	$\boldsymbol{V}_{13}$	$\boldsymbol{V}_2$	$\boldsymbol{V}_{14}$	$\boldsymbol{V}_3$	$\boldsymbol{V}_{15}$	$\boldsymbol{V}_4$	$\boldsymbol{V}_{16}$	$\boldsymbol{V}_5$	$\boldsymbol{V}_{17}$
−1	+1	$\boldsymbol{V}_3$	$\boldsymbol{V}_{15}$	$\boldsymbol{V}_4$	$\boldsymbol{V}_{16}$	$\boldsymbol{V}_5$	$\boldsymbol{V}_{17}$	$\boldsymbol{V}_6$	$\boldsymbol{V}_{18}$	$\boldsymbol{V}_1$	$\boldsymbol{V}_{13}$	$\boldsymbol{V}_2$	$\boldsymbol{V}_{14}$
	−1	$\boldsymbol{V}_5$	$\boldsymbol{V}_{17}$	$\boldsymbol{V}_6$	$\boldsymbol{V}_{18}$	$\boldsymbol{V}_1$	$\boldsymbol{V}_{13}$	$\boldsymbol{V}_2$	$\boldsymbol{V}_{14}$	$\boldsymbol{V}_3$	$\boldsymbol{V}_{15}$	$\boldsymbol{V}_4$	$\boldsymbol{V}_{16}$

Note: C_Ψ, C_T, and h_θ represent the torque hysteresis output, flux hysteresis output, and sector number of stator flux; +1/−1 represents increases/decreases in the torque and flux.

When the voltage drop of the stator resistance is disregarded, the relationships between the stator voltage and the change rates of the torque and flux can be derived as follows in accordance with Equs. (1)-(3):

$$\begin{cases} \dfrac{d}{dt}T_e = K\left(V_{n,y} - \omega_r|\boldsymbol{\Psi}_s|\right) \\ \dfrac{d}{dt}|\boldsymbol{\Psi}_s| = V_{n,x} \end{cases}, \tag{4}$$

where

$$K = \frac{3p}{2L_dL_q}[\psi_f L_q \cos\delta - |\boldsymbol{\Psi}_s|(L_q - L_d)\cos 2\delta]\cdot \tag{5}$$

According to Equ. (4), the change rates of the torque and flux of the PMSM are related to the y-axis and x-axis components of voltage vectors, respectively.

Based on the above analysis, the switching table of the standard DTC is as presented in Table II [8].

C. Neutral-Point Potential of 3L-DTC

The neutral-point current, i_O, may not be zero under the effects of SVs and MVs; as a result, the neutral-point potential changes. The variations in V_O in a control period can be expressed as follows [3]:

$$dV_O = \frac{T_s}{2C}\begin{bmatrix}|S_A - 1| & |S_B - 1| & |S_C - 1|\end{bmatrix}\begin{bmatrix} i_A \\ i_B \\ i_C \end{bmatrix}, \tag{6}$$

where C represents the capacitance of each capacitor. The effect of each SV and MV on V_O is only related to a certain phase current considering $i_A+i_B+i_C=0$. The effects of SVs and MVs are listed in Table III, where the shaded parts represent the MVs, "↑" indicates an increase, and "↓" indicates a decrease.

Table III shows that the MVs can render V_O uncontrollable, and the SVs correspond to two switching states with different effects on V_O. Therefore, the stable control of V_O can be realized by selecting the appropriate switching state of SVs that allows V_O to change to zero.

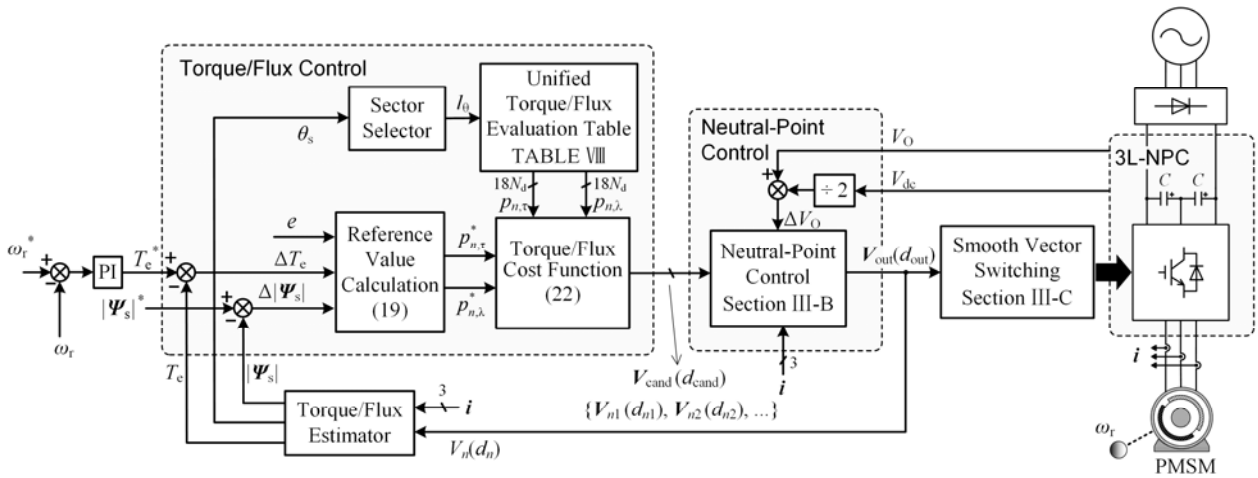

Fig. 3. Block diagram of the proposed algorithm.

TABLE III
RELATIONSHIP BETWEEN THE NEUTRAL-POINT POTENTIAL AND VOLTAGE VECTORS

$i_{ABC}(+/-)$	$V_O \downarrow$	$V_O \uparrow$
$i_A(+)$	$\boldsymbol{V}_7$ (100),$\boldsymbol{V}_{10}$(122) $\boldsymbol{V}_{14}$(120),$\boldsymbol{V}_{17}$(102)	$\boldsymbol{V}_7$ (211),$\boldsymbol{V}_{10}$(011)
$i_A(-)$	$\boldsymbol{V}_7$ (211),$\boldsymbol{V}_{10}$(011)	$\boldsymbol{V}_7$ (100),$\boldsymbol{V}_{10}$(122) $\boldsymbol{V}_{14}$(120),$\boldsymbol{V}_{17}$(102)
$i_B(+)$	$\boldsymbol{V}_9$ (010),$\boldsymbol{V}_{12}$(212) $\boldsymbol{V}_{13}$(210),$\boldsymbol{V}_{16}$(012)	$\boldsymbol{V}_9$ (121),$\boldsymbol{V}_{12}$(101)
$i_B(-)$	$\boldsymbol{V}_9$ (121),$\boldsymbol{V}_{12}$(101)	$\boldsymbol{V}_9$ (010),$\boldsymbol{V}_{12}$(212) $\boldsymbol{V}_{13}$(210),$\boldsymbol{V}_{16}$(012)
$i_C(+)$	$\boldsymbol{V}_8$ (221),$\boldsymbol{V}_{11}$(001) $\boldsymbol{V}_{15}$(021),$\boldsymbol{V}_{18}$(201)	$\boldsymbol{V}_8$ (110),$\boldsymbol{V}_{11}$(112)
$i_C(-)$	$\boldsymbol{V}_8$ (110),$\boldsymbol{V}_{11}$(112)	$\boldsymbol{V}_8$ (221),$\boldsymbol{V}_{11}$(001) $\boldsymbol{V}_{15}$(021),$\boldsymbol{V}_{18}$(201)

III. 3L-DTC-BASED EVALUATION TABLE

The proposed algorithm is established in this section. Its block diagram is shown in Fig. 3. It mainly consists of torque/flux control, neutral-point control, and smooth vector switching.

A. Torque/Flux Control

1) Evaluation Function of Torque/Flux: The 18 basic active vectors in 3L-NPC are expanded to infinite virtual vectors with adjustable magnitudes in their original direction by duty cycle modulation to increase the control precision and suppress the torque ripples. The uniform expression of these vectors can be expressed as follows:

$$\boldsymbol{V}_n(d_n)=\begin{cases}\dfrac{2}{3}V_{dc}d_n e^{j\theta_n}, n=1,2,...,6\\ \dfrac{1}{3}V_{dc}d_n e^{j\theta_n}, n=7,8,...,12\\ \dfrac{1}{\sqrt{3}}V_{dc}d_n e^{j\theta_n}, n=13,14,...,18\end{cases} \tag{7}$$

where θ_n represents the displacement angle between $\boldsymbol{V}_n$ and the α-axis, d_n represents the duty cycle of basic vector $\boldsymbol{V}_n$, and $d_n \in (0, 1]$.

The torque evaluation function, τ_n, and flux evaluation function, λ_n, with the variations d_n and θ_s are defined as follows:

$$\tau_n(d_n,\theta_s)=\frac{V_{n,y}(d_n,\theta_s)}{(2/3)V_{dc}}=\begin{cases}d_n\sin(\theta_n-\theta_s), & n=1,2,...,6\\ \dfrac{1}{2}d_n\sin(\theta_n-\theta_s), & n=7,8,...,12\\ \dfrac{\sqrt{3}}{2}d_n\sin(\theta_n-\theta_s), & n=13,14,...,18\end{cases}, \tag{8}$$

$$\lambda_n(d_n,\theta_s)=\frac{V_{n,x}(d_n,\theta_s)}{(2/3)V_{dc}}=\begin{cases}d_n\cos(\theta_n-\theta_s), & n=1,2,...,6\\ \dfrac{1}{2}d_n\cos(\theta_n-\theta_s), & n=7,8,...,12\\ \dfrac{\sqrt{3}}{2}d_n\cos(\theta_n-\theta_s), & n=13,14,...,18\end{cases}. \tag{9}$$

In accordance with Equs. (4), (8), and (9), the change rates of T_e and $|\boldsymbol{\Psi}_s|$ can be rearranged as follows:

$$\begin{cases}\dfrac{d}{dt}T_e=\dfrac{2V_{dc}K}{3}\left[\tau_n(d_n,\theta_s)-e\right]\\ \dfrac{d}{dt}|\boldsymbol{\Psi}_s|=\dfrac{2V_{dc}}{3}\lambda_n(d_n,\theta_s)\end{cases}, \tag{10}$$

where

$$e=\frac{\omega_r|\boldsymbol{\Psi}_s|}{(2/3)V_{dc}}. \tag{11}$$

The following expression can be obtained by simplifying Equ. (10):

$$\begin{cases}\dfrac{d}{dt}T_e\propto\tau_n(d_n,\theta_s)-e\\ \dfrac{d}{dt}|\boldsymbol{\Psi}_s|\propto\lambda_n(d_n,\theta_s)\end{cases}. \tag{12}$$

The values of $\tau_n(d_n, \theta_s)$–e and $\lambda_n(d_n, \theta_s)$ for each voltage vector are proportional to the change rates of the torque and flux, respectively. Thus, the torque and flux control effects of each voltage vector can be reflected by the evaluation functions τ_n and λ_n.

TABLE IV
EVALUATION FUNCTIONS OF 3L-NPC VECTORS

Vector No.		$\tau_n(d_n, \theta_s)$	$\lambda_n(d_n, \theta_s)$
LV	$\boldsymbol{V}_1$	$d_1\sin(-\theta_s)$	$d_1\cos(-\theta_s)$
	$\boldsymbol{V}_2$	$d_2\sin(\pi/3-\theta_s)$	$d_2\cos(\pi/3-\theta_s)$
	$\boldsymbol{V}_3$	$d_3\sin(2\pi/3-\theta_s)$	$d_3\cos(2\pi/3-\theta_s)$
	$\boldsymbol{V}_4$	$d_4\sin(\pi-\theta_s)$	$d_4\cos(\pi-\theta_s)$
	$\boldsymbol{V}_5$	$d_5\sin(4\pi/3-\theta_s)$	$d_5\cos(4\pi/3-\theta_s)$
	$\boldsymbol{V}_6$	$d_6\sin(5\pi/3-\theta_s)$	$d_6\cos(5\pi/3-\theta_s)$
SV	$\boldsymbol{V}_7$	$(1/2)\ d_7\sin(-\theta_s)$	$(1/2)\ d_7\cos(-\theta_s)$
	$\boldsymbol{V}_8$	$(1/2)\ d_8\sin(\pi/3-\theta_s)$	$(1/2)\ d_8\cos(\pi/3-\theta_s)$
	$\boldsymbol{V}_9$	$(1/2)\ d_9\sin(2\pi/3-\theta_s)$	$(1/2)\ d_9\cos(2\pi/3-\theta_s)$
	$\boldsymbol{V}_{10}$	$(1/2)\ d_{10}\sin(\pi-\theta_s)$	$(1/2)\ d_{10}\cos(\pi-\theta_s)$
	$\boldsymbol{V}_{11}$	$(1/2)\ d_{11}\sin(4\pi/3-\theta_s)$	$(1/2)\ d_{11}\cos(4\pi/3-\theta_s)$
	$\boldsymbol{V}_{12}$	$(1/2)\ d_{12}\sin(5\pi/3-\theta_s)$	$(1/2)\ d_{12}\cos(5\pi/3-\theta_s)$
MV	$\boldsymbol{V}_{13}$	$(\sqrt{3}/2)\ d_{13}\sin(\pi/6-\theta_s)$	$(\sqrt{3}/2)\ d_{13}\cos(\pi/6-\theta_s)$
	$\boldsymbol{V}_{14}$	$(\sqrt{3}/2)\ d_{14}\sin(\pi/2-\theta_s)$	$(\sqrt{3}/2)\ d_{14}\cos(\pi/2-\theta_s)$
	$\boldsymbol{V}_{15}$	$(\sqrt{3}/2)\ d_{15}\sin(5\pi/6-\theta_s)$	$(\sqrt{3}/2)\ d_{15}\cos(5\pi/6-\theta_s)$
	$\boldsymbol{V}_{16}$	$(\sqrt{3}/2)\ d_{16}\sin(7\pi/6-\theta_s)$	$(\sqrt{3}/2)\ d_{16}\cos(7\pi/6-\theta_s)$
	$\boldsymbol{V}_{17}$	$(\sqrt{3}/2)\ d_{17}\sin(3\pi/2-\theta_s)$	$(\sqrt{3}/2)\ d_{17}\cos(3\pi/2-\theta_s)$
	$\boldsymbol{V}_{18}$	$(\sqrt{3}/2)\ d_{18}\sin(11\pi/6-\theta_s)$	$(\sqrt{3}/2)\ d_{18}\cos(11\pi/6-\theta_s)$

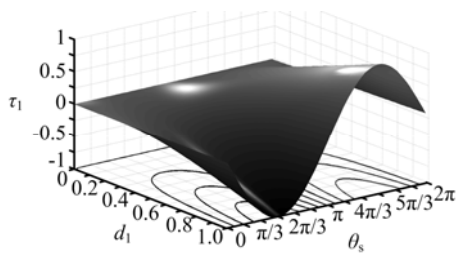

Fig. 4. 3D diagram of the torque evaluation of $\boldsymbol{V}_1$ with duty cycle.

The evaluation functions of all vectors are listed in Table IV. On the assumption that the values of d_n and θ_s are fixed, the relationships among the torque evaluation values and flux evaluation values of $\boldsymbol{V}_n(d_n)$ can be summarized as follows:

Corollary 1: The evaluation function values of the LVs are twice as high as those of the SVs in the same direction. For example, for $\boldsymbol{V}_1$ and $\boldsymbol{V}_7$, $\tau_1(d_1,\theta_s)=2\tau_7(d_7,\theta_s)$ and $\lambda_1(d_1,\theta_s)=2\lambda_7(d_7,\theta_s)$.

Corollary 2: The evaluation function values of the MVs are equal to those of their adjacent LVs. For example, for $\boldsymbol{V}_1$ and $\boldsymbol{V}_{13}$, $\tau_1(d_1,\theta_s)=2/\sqrt{3}\ \tau_{13}(d_{13},\theta_s+\pi/6)$ and $\lambda_1(d_1,\theta_s)=2/\sqrt{3}\ \lambda_{13}(d_{13},\theta_s+\pi/6)$.

Corollary 3: The relationships among the evaluation functions of the six LVs (SVs or MVs) can be derived as follows: $\tau_1(d_1,\theta_s)=\tau_n[d_n,\ \theta_s+(n-1)\pi/3]$ and $\lambda_1(d_1,\theta_s)=\lambda_n[d_n,\ \theta_s+(n-1)\pi/3]$, where n=2, 3,…, 6.

Corollary 4: The relationship between τ_n and λ_n is $\tau_n(d_n,\ \theta_s)=\lambda_n(d_n,\ \theta_s+\pi/2)$.

The formulas in Table IV suggest that τ_n and λ_n are determined by the duty cycle, d_n, and stator flux angle, θ_s. For τ_1 for example, the 3D diagram whose horizontal axis is d_1 and vertical axis is θ_s is shown in Fig. 4. The solid lines on the bottom surface are the isograms connecting the points with the same value of τ_1.

2) Unified Torque/Flux Evaluation Table: An offline unified torque/flux evaluation table is required to simplify the calculation process and reflect the control effects of the voltage vectors directly. The procedure for constructing this table is as follows: first, the value of d_n from 0 to 1 is equally divided into N_d pieces; thus, the basic vectors are expanded to 18 basic vectors and 18×(N_d−1) virtual vectors in their original directions. The α–β voltage complex plane is split into equal N_θ regions. Second, the average evaluation values of the vectors are calculated when the stator flux is located in different regions. The average torque evaluation value $\bar{\tau}_n$ and flux evaluation value $\bar{\lambda}_n$ can be respectively calculated by

$$\bar{\tau}_n(l_d,l_\theta)=\frac{N_\theta}{2\pi}\int_{\frac{2\pi}{N_\theta}(l_\theta-1)-\frac{\pi}{N_\theta}}^{\frac{2\pi}{N_\theta}l_\theta-\frac{\pi}{N_\theta}}\tau_n\left(\frac{l_d}{N_d},\theta_s\right)\mathrm{d}\theta_s\ , \tag{13}$$

$$\bar{\lambda}_n(l_d,l_\theta)=\frac{N_\theta}{2\pi}\int_{\frac{2\pi}{N_\theta}(l_\theta-1)-\frac{\pi}{N_\theta}}^{\frac{2\pi}{N_\theta}l_\theta-\frac{\pi}{N_\theta}}\lambda_n\left(\frac{l_d}{N_d},\theta_s\right)\mathrm{d}\theta_s\ , \tag{14}$$

where l_d and l_θ denote the numbers of duty cycles and sectors, respectively; N_d is a natural number; and N_θ is a multiple value of 12. The parameters l_d and l_θ are defined as

$$d_n=\frac{l_d}{N_d},\ l_d=1,\ 2,\ \ldots,\ N_d\ , \tag{15}$$

$$l_\theta=\begin{cases}1 & \theta_s>(2N_\theta-1)\pi/N_\theta \text{ or } \theta_s\le\pi/N_\theta\\ 2 & \pi/N_\theta<\theta_s\le 3\pi/N_\theta\\ \vdots & \vdots\\ N_\theta & (2N_\theta-3)\pi/N_\theta<\theta_s\le(2N_\theta-1)\pi/N_\theta\end{cases},\ 0\le\theta_s\le 2\pi\ . \tag{16}$$

Then, $\bar{\tau}_n(l_d,l_\theta)$ and $\bar{\lambda}_n(l_d,l_\theta)$ can be expanded R times and rounded as

$$p_{n,\tau}(l_d,l_\theta)=\mathrm{round}\left[R\cdot\bar{\tau}_n(l_d,l_\theta)\right], \tag{17}$$

$$p_{n,\lambda}(l_d,l_\theta)=\mathrm{round}\left[R\cdot\bar{\lambda}_n(l_d,l_\theta)\right], \tag{18}$$

where round[] represents the rounding of the number to the nearest integer and R can be selected as

$$R=\frac{M}{\max\left(\frac{N_\theta}{2\pi}\int_{\frac{2\pi}{N_\theta}(l_\theta-1)-\frac{\pi}{N_\theta}}^{\frac{2\pi}{N_\theta}l_\theta-\frac{\pi}{N_\theta}}\tau_n\left(\frac{l_d}{N_d},\theta_s\right)\mathrm{d}\theta_s\right)}\ . \tag{19}$$

In Equ. (19), M is a natural number, and the selection of R can ensure that $\bar{\tau}_n(l_d,l_\theta)$ and $\bar{\lambda}_n(l_d,l_\theta)$ are within the range of $-M$ to M.

TABLE V
TORQUE EVALUATION TABLE OF $\boldsymbol{V}_1$ WITH DUTY CYCLE

		l_θ											
		1	2	3	4	5	6	7	8	9	10	11	12
l_d/N_d	0.2	0	-1	-2	-2	-2	-1	0	1	2	2	2	1
	0.4	0	-2	-3	-4	-3	-2	0	2	3	4	3	2
	0.6	0	-3	-5	-6	-5	-3	0	3	5	6	5	3
	0.8	0	-4	-7	-8	-7	-4	0	4	7	8	7	4
	1.0	0	-5	-9	-10	-9	-5	0	5	9	10	9	5

TABLE VI
TORQUE EVALUATION TABLE OF $\boldsymbol{V}_7$ WITH DUTY CYCLE

0.5×		l_θ											
		1	2	3	4	5	6	7	8	9	10	11	12
l_d/N_d	0.2	0	-1	-2	-2	-2	-1	0	1	2	2	2	1
	0.4	0	-2	-3	-4	-3	-2	0	2	3	4	3	2
	0.6	0	-3	-5	-6	-5	-3	0	3	5	6	5	3
	0.8	0	-4	-7	-8	-7	-4	0	4	7	8	7	4
	1.0	0	-5	-9	-10	-9	-5	0	5	9	10	9	5

TABLE VII
TORQUE EVALUATION TABLE OF $\boldsymbol{V}_{13}$ WITH DUTY CYCLE

$(\sqrt{3}/2)\times$		l_θ											
		1	2	3	4	5	6	7	8	9	10	11	12
l_d/N_d	0.2	1	0	-1	-2	-2	-2	-1	0	1	2	2	2
	0.4	2	0	-2	-3	-4	-3	-2	0	2	3	4	3
	0.6	3	0	-3	-5	-6	-5	-3	0	3	5	6	5
	0.8	4	0	-4	-7	-8	-7	-4	0	4	7	8	7
	1.0	5	0	-5	-9	-10	-9	-5	0	5	9	10	9

On the basis of Equs. (12)-(18), the relationships between the change rates of torque/flux and $p_{n,\tau}(l_d,l_\theta)$ / $p_{n,\lambda}(l_d,l_\theta)$ can be expressed as

$$\begin{cases} \dfrac{\mathrm{d}}{\mathrm{d}t}T_e \approx \mathrm{avg}\left(\dfrac{\mathrm{d}}{\mathrm{d}t}T_e\right) \propto p_{n,\tau}(l_d,l_\theta) - Re \\ \dfrac{\mathrm{d}}{\mathrm{d}t}|\boldsymbol{\Psi}_s| \approx \mathrm{avg}\left(\dfrac{\mathrm{d}}{\mathrm{d}t}|\boldsymbol{\Psi}_s|\right) \propto p_{n,\lambda}(l_d,l_\theta) \end{cases} \tag{20}$$

On the basis of Equs. (13)-(18), the control effects of the vectors on the torque and flux can be subdivided into $2M$+1 evaluation levels by averaging and discretization. For $p_{1,\tau}$ for example, Fig. 4 can be simplified as Table V with M=10, N_d=5, and N_θ=12. The shade gradually changes from light to dark, indicating the gradual decline in $p_{1,\tau}(l_d, l_\theta)$. The same method can be used to obtain $p_{7,\tau}(l_d, l_\theta)$ and $p_{13,\tau}(l_d, l_\theta)$, as shown in Tables VI and VII, respectively. Vectors $\boldsymbol{V}_1$, $\boldsymbol{V}_7$, and $\boldsymbol{V}_{13}$ represent LVs, SVs, and MVs, respectively.

Tables V, VI, and VII present the following relationships: first, according to **Corollary 1**, the evaluation values of $\boldsymbol{V}_1$ are twice those of $\boldsymbol{V}_7$; thus, Table VI coincides with Table V if expanded twice. Second, according to **Corollary 2**, the evaluation values of $\boldsymbol{V}_{13}$ are equal to $\boldsymbol{V}_1$ when $\theta_s+\pi/6$ and then the evaluation values are multiplied $2/\sqrt{3}$ times. Thus, Table VII coincides with Table V by moving the row headers three cells to the left and expanding the values $2/\sqrt{3}$ times.

TABLE VIII
UNIFIED TORQUE/FLUX EVALUATION TABLE (N_d=5, M=10, AND N_θ=12)

		l_θ												
		$p_{13,\tau}(\cdot,2)$								$p_{15,\tau}(\cdot,2)$		$p_{14,\tau}(\cdot,2)$		
MV $(\sqrt{3}/2)\times$	$\boldsymbol{V}_{15}$	6	7	8	9	10	11	12	1	2	3	4	5	Torque
	$\boldsymbol{V}_{14}$	4	5	6	7	8	9	10	11	12	1	2	3	
	$\boldsymbol{V}_{13}$	2	3	4	5	6	7	8	9	10	11	12	1	
SV 0.5×	$\boldsymbol{V}_9$	5	6	7	8	9	10	11	12	1	2	3	4	
	$\boldsymbol{V}_8$	3	4	5	6	7	8	9	10	11	12	1	2	
	$\boldsymbol{V}_7$	1	2	3	4	5	6	7	8	9	10	11	12	
LV	$\boldsymbol{V}_3$	5	6	7	8	9	10	11	12	1	2	3	4	
	$\boldsymbol{V}_2$	3	4	5	6	7	8	9	10	11	12	1	2	
	$\boldsymbol{V}_1$	1	2	3	4	5	6	7	8	9	10	11	12	
l_d/N_d	0.2	0	-1	-2	-2	-2	-1	0	1	2	2	2	1	Evaluation
	0.4	0	-2	-3	-4	-3	-2	0	2	3	4	3	2	
	0.6	0	-3	-5	-6	-5	-3	0	3	5	6	5	3	
	0.8	0	-4	-7	-8	-7	-4	0	4	7	8	7	4	
	1.0	0	-5	-9	-10	-9	-5	0	5	9	10	9	5	
LV	$\boldsymbol{V}_1$	4	5	6	7	8	9	10	11	12	1	2	3	
	$\boldsymbol{V}_2$	6	7	8	9	10	11	12	1	2	3	4	5	
	$\boldsymbol{V}_3$	8	9	10	11	12	1	2	3	4	5	6	7	
SV 0.5×	$\boldsymbol{V}_7$	4	5	6	7	8	9	10	11	12	1	2	3	
	$\boldsymbol{V}_8$	6	7	8	9	10	11	12	1	2	3	4	5	
	$\boldsymbol{V}_9$	8	9	10	11	12	1	2	3	4	5	6	7	
MV $(\sqrt{3}/2)\times$	$\boldsymbol{V}_{13}$	5	6	7	8	9	10	11	12	1	2	3	4	Flux
	$\boldsymbol{V}_{14}$	7	8	9	10	11	12	1	2	3	4	5	6	
	$\boldsymbol{V}_{15}$	9	10	11	12	1	2	3	4	5	6	7	8	
		l_θ												
		$p_{15,\lambda}(\cdot,2)$								$p_{14,\lambda}(\cdot,2)$		$p_{13,\lambda}(\cdot,2)$		

Similarly, the torque/flux evaluation table of the 18 basic vectors and 18×(N_d−1) virtual vectors coincide with Table V by translation and scaling. Subsequently, a unified torque/flux table similar to Table VIII can be obtained. This table includes the torque/flux evaluation values of the nine basic vectors and their corresponding virtual vectors. The remaining nine active vectors are located in the opposite directions of the vectors in Table VIII; thus, their evaluation values can be obtained by reversing the values in Table VIII. The shaded area in Table VIII corresponds to the evaluation values.

On the assumption that the stator flux is located in region l_θ, the values of all the vectors with different duty cycles can be obtained by looking up Table VIII. For example, $\boldsymbol{V}_{13}(d_{13})$ can increase the flux modulus when the stator flux is located in region 2, and the flux evaluation value is $8\times(\sqrt{3}/2)=4\sqrt{3}$ when the duty cycle is 0.8 (l_d=4). By contrast vector $\boldsymbol{V}_{16}(d_{16})$ can reduce the flux modulus, which has an opposite direction compared with $\boldsymbol{V}_{13}(d_{13})$. Therefore, its flux evaluation value is $-8\times(\sqrt{3}/2)=-4/\sqrt{3}$ with the same duty cycle.

3) Torque/Flux Reference Value Calculation: The torque and flux reference values can be calculated on the basis of their tracking errors. With Equ. (20) as basis, the torque and flux reference values can be expressed as follows:

$$\begin{cases} p^*_{n,\tau}(l_d,l_\theta)=\dfrac{\Delta T_e}{K_T}+Re \\ p^*_{n,\lambda}(l_d,l_\theta)=\dfrac{\Delta|\boldsymbol{\Psi}_s|}{K_\Psi} \end{cases}, \quad (21)$$

where K_T and K_Ψ are the control parameters of torque and flux, respectively, and K_T, K_Ψ>0. Excessively high or inappropriately low K_T and K_Ψ can lead to the control failure of torque and flux. The tuning methods for K_T and K_Ψ are detailed in Section IV-B.

The selection of the candidate vectors is as follows: first, the evaluation values of all the vectors with different duty cycles should be obtained by looking up Table VIII because their effects on torque and flux differ. Second, the values need to be substituted into the cost function *f*.

$$f=\varepsilon_T\left|p^*_{n,\tau}(l_d,l_\theta)-p_{n,\tau}(l_d,l_\theta)\right|+\varepsilon_\Psi\left|p^*_{n,\lambda}(l_d,l_\theta)-p_{n,\lambda}(l_d,l_\theta)\right|, \quad (22)$$

where $p^*_{n,\tau}(l_d,l_\theta)$ and $p^*_{n,\lambda}(l_d,l_\theta)$ can be determined by Equ. (21) and ε_T and ε_Ψ are the weight factors, which are non-negative dimensionless coefficients. The values of ε_T and ε_Ψ decide the significance of torque and flux in the control process, respectively. For example, when the ratio of the weight factors ε_T:ε_Ψ is 2:1, the significance of the torque control is twice that of the flux control. Both ε_T and ε_Ψ are tuned on the basis of the actual control requirement. In this study, the ratio of weight the factors ε_T:ε_Ψ is 1:1.

The cost function should be calculated $18\times N_d$ times in each control period. The vectors that minimize *f* are selected as the candidate vectors, which are denoted by $\boldsymbol{V}_{cand}(d_{cand})$ { $\boldsymbol{V}_{n1}(d_{n1})$, $\boldsymbol{V}_{n2}(d_{n2})$, … }. The candidate vectors are not unique, thereby allowing for neutral-point potential control.

B. Neutral-Point Control

Multiple candidate vectors can be identified for torque and flux control, but these vectors have different effects on the neutral-point potential. The balance of the neutral-point potential and the optimal control of torque and flux can be realized simultaneously by selecting the vector that changes the neutral-point potential to zero.

The situations of the candidate vectors can be divided into the following three categories according to the number of the candidate vectors:

(1) One candidate vector. Obviously, this candidate vector will be selected as the output vector. In this situation, the neutral-point potential can be controlled if the optimum vector is an SV. The corresponding switching state of the SV that can balance the neutral-point potential will likewise be selected. However, the neutral-point potential cannot be controlled if the candidate vector is an LV or an MV.

(2) Two candidate vectors. If an SV is included in the candidate vectors, then the SV will be selected as the output vector. If the two candidate vectors are an LV and an MV, then the MV should be selected as the output vector if it allows the neutral-point potential to change to zero; otherwise, the LV will be selected as the output vector.

(3) Three or more candidate vectors. In this situation, the output vector should be selected in the following order: SV, MV that can change the neutral-point potential to zero, and LV.

TABLE IX
RATED PARAMETERS OF THE PMSM

Parameter	Symbol	Unit	Value
Number of pole pairs	p	—	8
Permanent magnet flux	ψ_f	Wb	0.9031
Stator resistance	R_s	Ω	0.76
d-Axis inductance	L_d	mH	13.0
q-Axis inductance	L_q	mH	13.0
Rated speed	n_N	r/min	300
Rated torque	T_N	Nm	192
Rated voltage	U_N	V	380

C. Smooth Vector Switching

After the output vector $\boldsymbol{V}_{out}$ and its duty cycle d_{out} have been determined, a PWM modulator is used for duty cycle generation and smooth vector switching by inserting $\boldsymbol{V}_0$, whose vector state is 111, at both the beginning and end of the output vector.

When the motor operates in the steady state, several consecutive vectors with unity duty cycle cause large torque and flux ripples and a “high voltage jump” in a bridge arm. For this reason, the values of K_T and K_Ψ should be selected appropriately to ensure that the duty cycle of the output vector is less than 1.0.

IV. SIMULATION ANALYSIS

The performance of the proposed method is analyzed using MATLAB/Simulink. The parameters of the PMSM are shown in Table IX. The torque and flux ripples are evaluated in terms of their standard deviations σ_T and σ_Ψ, respectively. These standard deviations are expressed as follows:

$$\sigma_x=\sqrt{\frac{1}{n-1}\sum_{i=1}^{n}\left(x_i-\bar{x}\right)^2}, \quad \bar{x}=\frac{1}{n}\sum_{i=1}^{n}x_i, \quad (23)$$

where *n* is the number of samples.

A. Influences of M and N_d

Fig. 5 shows the σ_T, σ_Ψ, and the deviation of the neutral-point potential (ΔV_O) of the proposed approach with M=3, 4, …, 10 and N_d=2, 3, …, 10. In the simulation, the speed reference is n_r=150r/min, the load torque is T_L=100Nm, and N_θ=12. As shown in Figs. 5(a)-(c), as M and N_d increase, the undesired torque and flux ripples and neutral-point potential deviation decrease. This outcome is attributed to the accuracy of the effects of the vectors on PMSM described by the evaluation table when M and N_d increase continually.

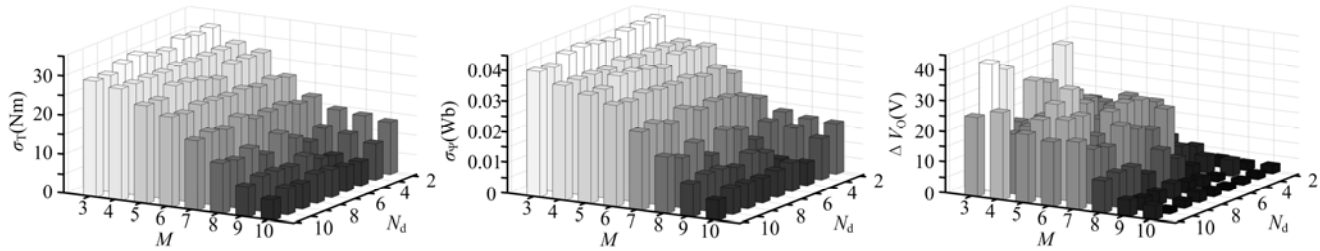

(a) (b) (c)

Fig. 5. Simulation results of the proposed approach with different M and N_d values. (a) Standard deviation of torque, σ_T. (b) Standard deviation of flux, σ_Ψ. (c) Deviation of the neutral-point potential, ΔV_O.

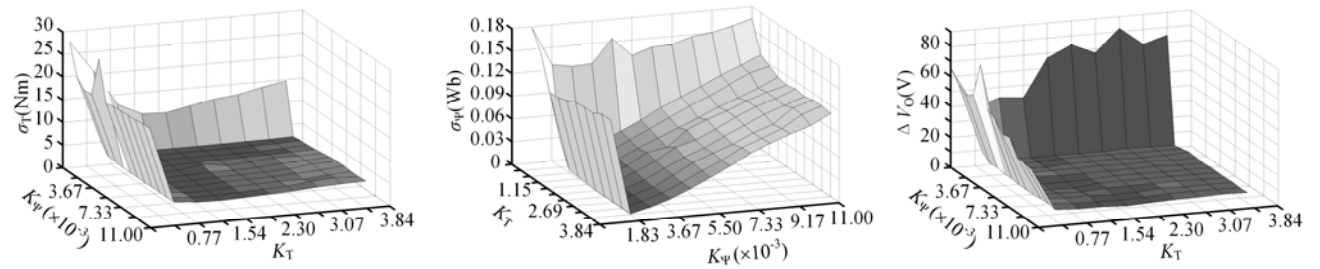

(a) (b) (c)

Fig. 6. Simulation results of the proposed approach with different K_T and K_Ψ Values. (a) Standard deviation of torque, σ_T. (b) Standard deviation of flux, σ_Ψ. (c) Deviation of the neutral-point potential, ΔV_O.

Furthermore, more SVs with different duty cycles can be selected to balance the neutral-point potential. However, the storage space occupied by the evaluation table in the digital controller increases with increasing M and N_d. Thus, the values of M and N_d should be set by considering both the storage space and the system performance. In the following simulation and experiments, M=10 and N_d=10.

B. Influences of K_T and K_Ψ

On the basis of Equ. (21), the appropriate K_T and K_Ψ are analyzed as follows:

(1) If K_T, $K_\Psi \to 0$, then $p^*_{n,\tau}$ and $p^*_{n,\lambda}$ are greater than M or smaller than $-M$. In this situation, $p^*_{n,\tau}$ and $p^*_{n,\lambda}$ are selected as their maximum or minimum values in the evaluation table. As a result, undesired torque and flux ripples occur in the steady state. Moreover, the deviation of the neutral-point potential becomes large because the SVs in the evaluation table are not selected.

(2) If K_T, $K_\Psi \to \infty$, then $p^*_{n,\tau}$ and $p^*_{n,\lambda}$ are approximate to zero. In this situation, only the SVs are selected as the candidate vectors, and the feedback of torque and that of flux do not influence $p^*_{n,\tau}$ and $p^*_{n,\lambda}$, respectively. As a result, tracking errors and large ripples of torque and flux are yielded. However, the neutral-point potential is nearly balanced.

(3) If T_e and $|\boldsymbol{\Psi}_s|$ track their references, ΔT_e, $\Delta|\boldsymbol{\Psi}_s|$, and ΔV_O oscillate in the vicinity of zero. The control parameters K_T and K_Ψ are tuned as follows, with K_T as an example. The maximum torque ripple is assumed to be $\delta_T T_N$ in the steady state, where $\delta_T > 0$ and T_N is the rated torque. When $\Delta T_e = \pm\delta_T T_N$, K_T should ensure that $p^*_{n,\tau} - Re \approx \pm M$, then the proper value of K_T is

$$K_T = \frac{\delta_T T_N}{M}. \tag{24}$$

In the same way, proper K_Ψ can be approximately set to

$$K_\Psi = \frac{\delta_\Psi \psi_f}{M} \tag{25}$$

where $\delta_\Psi \psi_f$ is the maximum flux ripple in the steady state.

Fig. 6 shows the simulated σ_T, σ_Ψ, and ΔV_O values with different K_T and K_Ψ values. In the simulation, M=10, N_d=10, n_r=150r/min, T_L=100Nm, and N_θ=12. As δ_T increases from 2% to 20% and δ_Ψ increases from 1% to 12%, K_T increases from 0.38 to 3.84, and K_Ψ increases from 0.001 to 0.011. As shown in Fig. 6(a), an increase in K_T results in an L-shaped relationship between σ_T and K_T, whereas an increase in K_Ψ cannot cause a significant variation in σ_T. The same trend is observed for σ_Ψ, as shown in Fig. 6(b). As shown in Fig. 6(c), an L-shaped relationship between ΔV_O and K_T/K_Ψ is likewise observed. However, ΔV_O monotonically decreases as K_T and K_Ψ increase. When K_T and K_Ψ are tuned, the σ_T and σ_Ψ in the corner of the L-shaped surface of Fig. 6(a) can be selected, respectively. In this paper, K_T=0.69 and K_Ψ=0.0028 (K_T and K_Ψ are rounded to two significant figures).

V. Experimental Results

The feasibility and effectiveness of the proposed algorithm are verified through experiments on the standard DTC [8] and

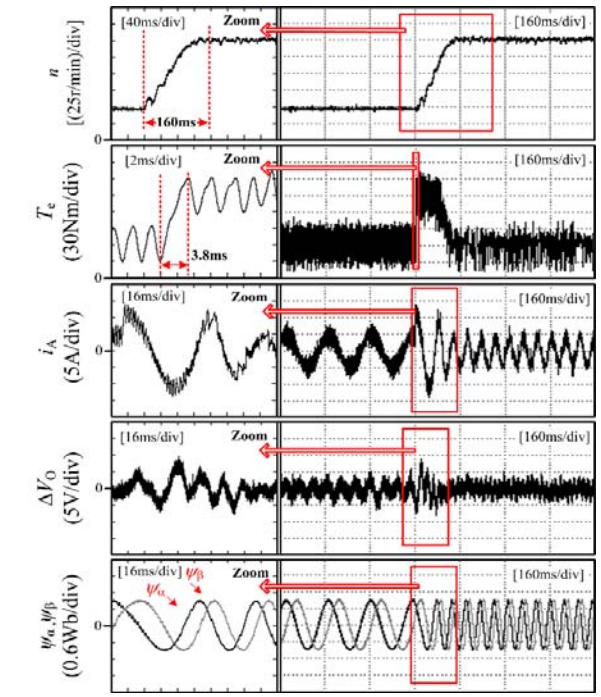

(a)

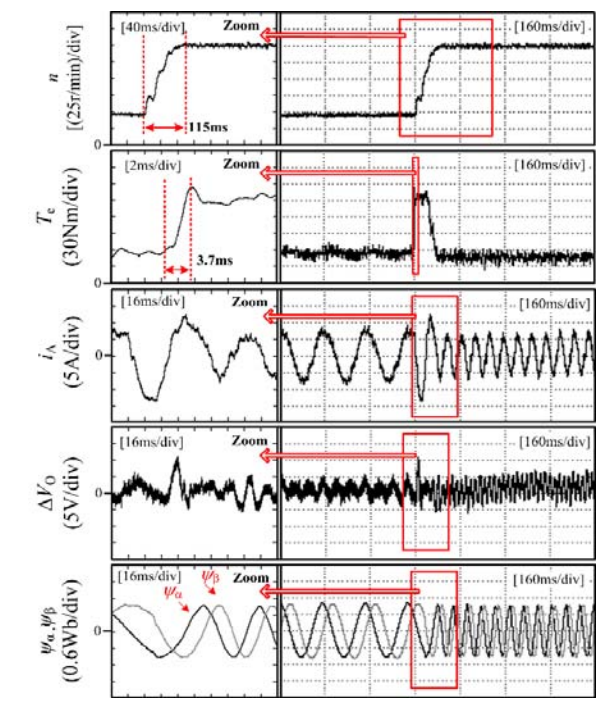

(b)

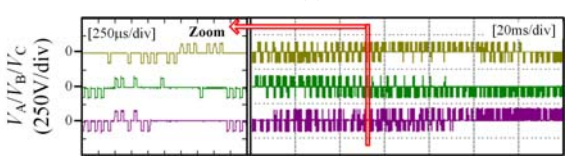

(c)

Fig. 7. Experimental waveforms of the speed, torque, stator current, deviation of the neutral-point potential, and flux α–β components of (a) the standard DTC and (b) the proposed algorithm. (c) Stator phase voltage.

TABLE X
COMPARISON OF THE DYNAMIC EXPERIMENTAL RESULTS OF THE STANDARD DTC AND THE PROPOSED ALGORITHM

Item	T_{sc} (μs)	Dynamic performance		
		t_T (ms)	t_V (ms)	V_O (V)
Standard DTC	80	3.8	160	10
DTC with duty cycle	200	3.7	115	10

the proposed algorithm are conducted. The parameters of the PMSM are listed in Table IX. The following experimental conditions are applied: $|\boldsymbol{\Psi}_s|^*$=0.9Wb, M=10, N_d=10, N_θ=12, K_T=0.69, K_Ψ=0.0028, ε_T:ε_Ψ=1:1. The flux and torque hysteresis bands of the standard DTC are set to $0.021\psi_f$ and $0.026T_N$ in our experiments, respectively. Table II is used as the switching table.

A. Dynamic Performance

Fig. 7 shows the waveforms of the speed, electromagnetic torque, stator current, deviation of the neutral-point potential, and α–β components of the stator flux linkage of both methods when the speed reference, n_r, is increased from 50r/min to 150r/min and the load torque T_L is 50Nm. A comparison of the results of the standard DTC and proposed algorithm in the dynamic experiments is presented in Table X. As shown, the torque response time of both methods are nearly equal, indicating that the proposed algorithm inherits the advantage of rapid dynamic torque response of the standard DTC. The deviations of the neutral-point potentials of both methods are equal, suggesting that the proposed method can also balance the neutral-point potential when the motor is dynamic. The speed response time, t_v, of the proposed algorithm is 35ms shorter than that of the standard DTC. This result is because the torque of the algorithm is smooth and the motor is operating smoothly.

The smooth vector switching of the proposed algorithm is likewise verified. Fig. 7(c) shows the experimental waveforms of the stator phase voltage. As shown, in the phase voltage u_A, a switching function with a voltage level of 1 is inserted to prevent the voltage level from jumping from 0 to 2. The jump in the voltage level from 0 to 2 does not occur under the dynamic condition. The voltage level of the switching function changes as follows: 2→1, 1→2, 0→1, or 1→0.

B. Steady-State Performance

Fig. 8 shows the waveforms of the stator flux modulus, electromagnetic torque, deviation of the neutral-point potential, and stator current of the standard DTC and proposed algorithm in the steady state, with n_r being 100r/min and T_L being 100Nm. A comparison of the results of the standard DTC and the proposed algorithm is presented in Table XI. The control periods are 80μs and 200μs for the standard DTC and proposed algorithm, respectively, to ensure that the switching frequencies of both methods are approximately equal. As

TABLE XI
COMPARISON OF THE RESULTS OF THE COMPARED METHODS IN THE STEADY-STATE EXPERIMENT

Item	T_{sc} (μs)	f_{av} (kHz)	T_L=100Nm and n_r=100r/min			T_L=50Nm and n_r=50r/min			T_L=50Nm and n_r=150r/min		
			σ_T (Nm)	σ_Ψ (Wb)	V_O (V)	σ_T (Nm)	σ_Ψ (Wb)	V_O (V)	σ_T (Nm)	σ_Ψ (Wb)	V_O (V)
Standard DTC	80	2.23	21.06	0.018	±5	23.37	0.024	±5	21.19	0.022	±5
DTC with duty cycle	200	1.98	6.63	0.024	±5	8.07	0.029	±4	9.81	0.031	±6

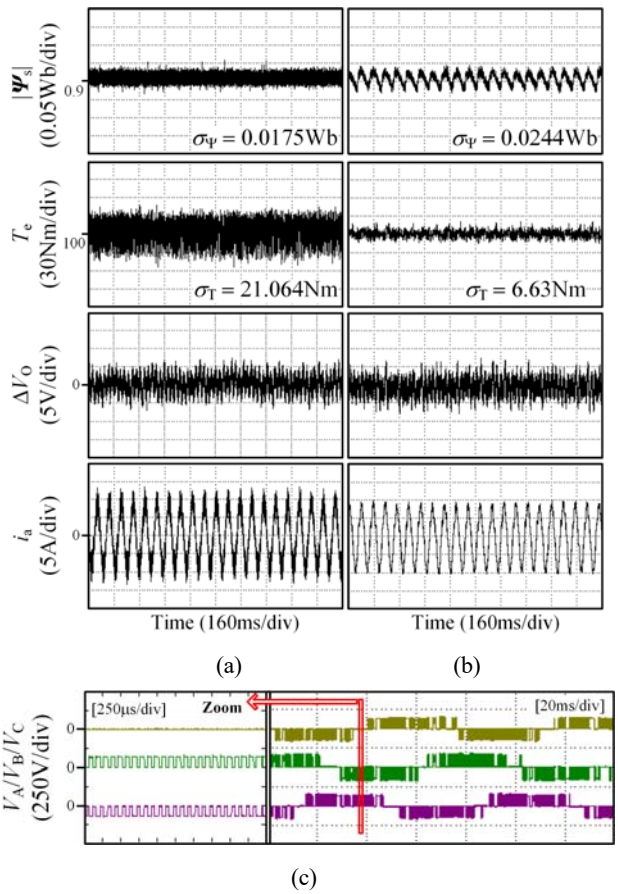

Fig. 8. Experimental waveforms of the stator flux modulus, torque, deviation of the neutral-point potential, and stator current of (a) the proposed algorithm and (b) the standard DTC. (c) Stator phase voltage.

shown in Table XI, the torque standard deviation σ_T of the proposed algorithm is remarkably reduced compared with that of the standard DTC. Thus, the torque control performance of the proposed algorithm is considerably better than that of the standard DTC. The proposed algorithm exerts the same control effects on the neutral-point potential as those of the standard DTC. Additionally, the deviations of the neutral-point potential are small.

The smooth vector switching of the proposed algorithm is also verified in the steady state. Fig. 8(c) shows the experimental waveforms of the stator phase voltage. As shown in Fig. 8(c), the jump in the voltage level from 0 to 2 does not occur under the steady-state condition. The voltage level of the switching function changes as follows: 2→1, 1→2, 0→1, or 1→0.

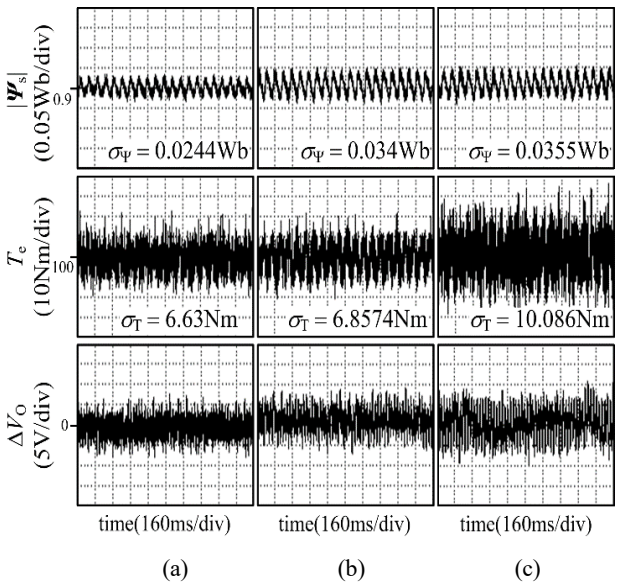

Fig. 9. Experimental waveforms of the stator flux modulus, torque, and deviation of the neutral-point potential with (a) M=10 and N_d=10; (b) M =7 and N_d=7; (c) M=5; N_d=5.

C. Influences of M and N_d

Fig. 9 shows the waveforms of the stator flux modulus, electromagnetic torque, and deviation of the neutral-point potential of the proposed algorithm with different M and N_d values. The fluctuations in the torque, flux, and deviation of the neutral-point potential are reduced with increases in M and N_d. The experimental results are in accordance with the simulation results in Section IV-A.

D. Influences of K_T and K_Ψ

Fig. 10 shows the waveforms of the stator flux modulus, electromagnetic torque, and deviation of the neutral-point potential of the proposed algorithm with different K_T and K_Ψ values. The torque and flux ripples increase when the K_T and K_Ψ are inappropriately selected.

However, the control of the neutral-point potential improves with relatively large K_T and K_Ψ. The experimental results are in accordance with the simulation results in Section IV-B.

E. Influence of ε_T:ε_Ψ

Fig. 11 shows a tradeoff exists between torque control and

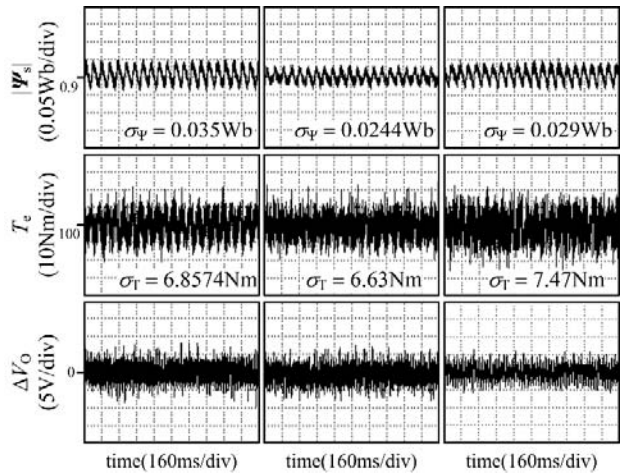

(a) (b) (c)

Fig. 10. Experimental waveforms of the stator flux modulus, torque, and deviation of the neutral-point with (a) K_T=0.62 and K_Ψ=0.0025; (b) K_T=0.69 and K_Ψ=0.0028; (c) K_T=0.75 and K_Ψ=0.0030.

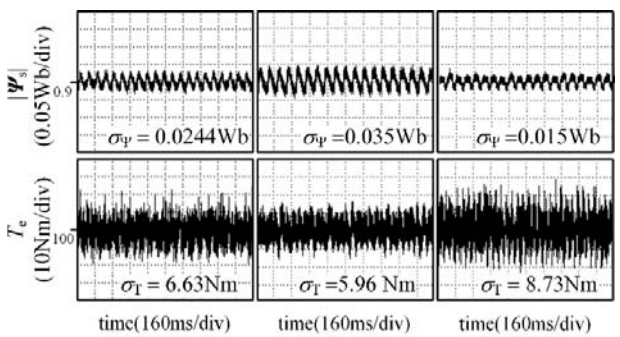

(a) (b) (c)

Fig. 11. Experimental waveforms of the stator flux modulus and torque with (a) ε_T:ε_Ψ=1:1; (b) ε_T:ε_Ψ=2:1; (c) ε_T:ε_Ψ=1:2.

flux control. The control effects of the output vector on the torque and flux can be enhanced by increasing the values of ε_T and ε_Ψ, respectively.

VI. Conclusions

In this paper, a novel duty-cycle modulation-based DTC algorithm has been proposed for 3L-NPC-fed PMSM drives. The experimental results indicate that the proposed algorithm inherits the rapid dynamic torque response of the standard DTC algorithm. Furthermore, the torque ripples in the steady state are reduced effectively, and both neutral-point potential balance and smooth vector switching are ensured. The outstanding characteristics of the proposed algorithm are summarized as follows:

1) The unified torque/flux evaluation table with multiple voltage vectors and precise control levels is an effective extension of the standard DTC switching table of a 3L-NPC. It contains 18 basic voltage vectors and $18\times(N_d-1)$ virtual voltage vectors with fixed direction and amplitude. These vectors are synthesized using the PWM principle. The effects of all of these vectors on torque and flux are divided into $2M$+1 levels, and these effects are independent of the parameters of the motor. Therefore, the unified torque/flux evaluation table is universal for the DTC of different power levels. The values in the table represent the torque and flux change rates caused by the $18\times N_d$ vectors.
2) The candidate vectors are selected on the basis of the cost function. The cost function is used to evaluate the effects of the $18\times N_d$ voltage vectors on the torque and flux. The candidate vectors that minimize the cost function are selected. Several candidate vectors with the same cost function value can be selected on the basis of the operating conditions. Therefore, the effects of these vectors on the torque and flux of the motor are the same.
3) The mechanism for the neutral-point potential balance is established. A vector is selected from the candidate vectors to control the motor depending on the demand to increase or decrease the neutral-point potential. Thus, the selected vector not only allows for torque and flux control but also neutral-point potential balance.

Acknowledgment

The authors are grateful to the Key Project in the Science & Technology Pillar Program of Tianjin (16YFZCSF00580) and the Research Fund for the National Natural Science Foundation of China (51377121) for supporting this work.

References

[1] M. H. Vafaie, B. M. Dehkordi, P. Moallem, and A. Kiyoumarsi, "A new predictive direct torque control method for improving both steady-state and transient-state operations of the PMSM," *IEEE Trans. Power Electron.*, Vol. 31, No. 5, pp. 3738-3753, May. 2016.
[2] Y. S. Choi, H. H. Choi, and J. W. Jung, "Feedback linearization direct torque control with reduced torque and flux ripples for IPMSM drives," *IEEE Trans. Power Electron.*, Vol. 31, No. 5, pp. 3728-3737, May. 2016.
[3] C. L. Xia, Z. Xu, and J. X. Zhao, "A new direct power control strategy for NPC three-level voltage source rectifiers using a novel vector influence table method," *Journal of Power Electronics*, Vol.15, No.1, pp. 106-115, Jan. 2015.
[4] J. Lyu, W. B. Hu, F. Y. Wu, K. Yao, and J. J. Wu, "A new DPWM method to suppress the low frequency oscillation of the neutral-point voltage for NPC three-level inverters," *Journal of Power Electronics*, Vol. 15, No. 5, pp. 1207-1216, Sep. 2015.
[5] W. Chen, H. W. Sun, X. Gu, and C. L. Xia, "Synchronized space-vector PWM for three-level VSI with lower harmonic distortion and switching frequency," *IEEE Trans. Power Electron.*, Vol. 31, No. 9, pp. 6428-6441, Sep. 2016.
[6] P. Van-Tien, T. Q. Zheng, Z. P. Yang, F. Lin, and V. D. Do, "A DTC stator flux algorithm for the performance improvement of induction traction motors," *Journal of Power Electronics*, Vol. 16, No. 2, pp. 572-583, Mar. 2016.

[7] A. H. Abosh, A. Q. Zhu, and Y. Ren, "Reduction of torque and flux ripples in space-vector modulation based direct torque control of asymmetric permanent magnet synchronous machine," *IEEE Trans. Power Electron.*, Vol. 32, No. 4, pp. 2976-2986, Apr. 2016.
[8] Y. C. Zhang, J. G. Zhu, Z. M. Zhao, W. Xu, and D. G. Dorrell, "An improved direct torque control for three-level inverter-fed induction motor sensorless drive," *IEEE Trans. Power Electron.*, Vol. 27, No. 3, pp. 1502-1513, Mar. 2012.
[9] Y. D. Li, X. Hou, and Z. H. Tan, "Direct torque control of induction motor fed by three level inverter（II）- method of synthesizing vectors," *Transactions of China Electrotechnical Society*, Vol. 19, No. 5, pp. 31-35, May 2004.
[10] D. Casadei, G. Serra, and A. Tani, "Direct torque control for induction machines: a technology status review," in *Proc. WEMDCD*, pp. 117-129, 2013.
[11] K. B. Lee, J. H. Song, I. Choy, and J. Y. Yoo, "Improvement of low-speed operation performance of DTC for three-level inverter-fed induction motors," *IEEE Trans. Ind. Electron.*, Vol. 48, No. 5, pp. 1006-1014, Oct. 2001.
[12] S. Mukherjee and G. Poddar, "Direct torque control of squirrel cage induction motor for optimum current ripple using three-level inverter," *IET Power Electron.*, Vol. 3, No. 6, pp. 904-914, Nov. 2010.
[13] D. Mohan, X. Zhang, and G. H. B. Foo, "Three level inverter fed direct torque control of IPMSM with constant switching frequency and torque ripple reduction," *IEEE Trans. Ind. Electron.*, Vol. 63, No.12, pp. 7908-7918, Dec. 2016.
[14] L. Lin, Y. P. Zou, H. Q. Zhong, X. D. Zou, J. Zhang, X. Zhang, and C. X. Huang, "DTC algorithm of induction motors fed by three-level inverter based on fixed synthesizing vector," in *Proc. of the CSEE*, Vol. 28, No. 27, pp.120-125, Sep. 2008.
[15] K. B. Lee, J. H. Song, I. Choy, and J. Y. Yoo, "Torque ripple reduction in DTC of induction motor driven by three-level inverter with low switching frequency," *IEEE Trans. Power Electron.*, Vol. 17, No. 2, pp. 255-264, Mar. 2002.
[16] G. Brando, A. Dannier, A. D. Pizzo, R. Rizzo, and I. Spina, "Generalised look-up table concept for direct torque control in induction drives with multilevel inverters," *IET Electric Power Appl.*, Vol. 9, No. 8, pp. 556-567, Sep. 2015.
[17] C. L. Xia, S. Wang, X. Gu, Y. Yan, and T. N. Shi, "Direct torque control for VSI-PMSM using vector evaluation factor table," *IEEE Trans. Ind. Electron.*, Vol. 63 No. 7, pp. 4571-4583, Jul. 2016.

Wei Chen (M'12) was born in Shanxi, China, in 1977. He received his B.S., M.S., and Ph.D. degrees in Electrical Engineering from Tianjin University, Tianjin, China, in 2000, 2003, and 2006, respectively. In 2006, he was a lecturer at Tianjin University, where he has been an associate professor at the School of Electrical and Information Engineering since 2009. His research interests include optimization modeling of electrical machines and drives.

Ying-Ying Zhao was born in Hebei, China, in 1989. She received her B.S. degree from Shijiazhuang Tiedao University, China, in 2013, and M.S. degree from Tianjin University, China, in 2017, both in Electrical Engineering. Her research interest is the control of three-level inverter-fed PMSM drives.

Zhan-Qing Zhou was born in Ningxia, China, in 1989. In 2010, he received his B.S. degree from Tianjin University, Tianjin, China, where he is currently working toward the Ph.D. degree in Electrical Engineering at the School of Electrical and Information Engineering. His research interests include model predictive control of power electronics and electrical drives.

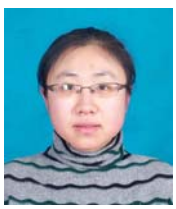

Yan Yan was born in Tianjin, China, in 1981. She received her B.S. and M.S. degrees in Electrical Engineering Tianjin University of Science and Technology, Tianjin, China, in 2004 and 2007, respectively, and Ph.D. degree in the same program from Tianjin University, Tianjin, China, in 2010. She is currently a lecturer at the School of Electrical and Information Engineering, Tianjin University, Tianjin, China. Her research interests include the design and control of matrix converters for electrical drive applications and power converters for wind power generation.

Chang-Liang Xia was born in Tianjin, China, in 1968. He received his B.S. degree in Electrical Engineering from Tianjin University, China, in 1990. He received his M.S. and Ph.D. degrees in Electrical Engineering from Zhejiang University, China, in 1993 and 1995, respectively. He is currently a professor at the School of Electrical and Information Engineering, Tianjin University, as well as at the Tianjin Engineering Center of Electric Machine System Design and Control, Tianjin Polytechnic University. In 2008, he was awarded "Yangtze Fund Scholar" Distinguished Professor. He is currently supported by the National Science Fund for Distinguished Young Scholars. His current research interests include electrical machines and their control systems, power electronics, and control of wind generators.